Research Article

Synthesis and characterization of $K_2Pr_2O(BO_3)_2$: structural, spectroscopic and thermogravimetric investigations of a novel potassium praseodymium oxoborate structure-type

Pengyun Chen[1] · M. Mangir Murshed[1,2] · Thorsten M. Gesing[1,2]

Abstract

Single crystal and polycrystalline powder samples of a new potassium praseodymium oxoborate $K_2Pr_2O(BO_3)_2$ were prepared by high-temperature solid-state methods. The crystal structure obtained from single-crystal X-ray diffraction data was confirmed by powder X-ray data Rietveld refinement ($P2_1/c$, $a = 1135.00(3)$ pm, $b = 660.64(2)$ pm, $c = 1072.03(3)$ pm, $\beta = 117.128(2)°$, $V = 715.41(3) \times 10^6$ pm^3). The bond-valence sum of the central cation for $KO_{6/7}$, PrO_9 and BO_3 coordination lies close to the respective empirical value. Both Fourier-transform infrared and Raman spectroscopy demonstrated the vibrational features of the isolated BO_3 planar group. The diffuse UV/Vis reflectance spectra showed fundamental absorption edge at 4.49(1) eV obtained from the combined approach using Tauc and derivation of absorption spectrum fitting methods. The greenish color of the sample was identified originating from $4f$–$4f$-electron transitions. The thermal stability was investigated by using simultaneous thermogravimetric analysis and differential scanning calorimetry. The decomposed products $Pr_{26}O_{27}(BO_3)_8$ (90(2) wt%) and Pr_6O_{11} (10(2) wt%) were confirmed by powder X-ray diffraction data analysis, complementary to the weight-loss during the heating process. Since Pr^{3+} cation is known to show interesting photoluminescence property, this novel compound may be a prospective candidate as phosphor.

Keywords Potassium praseodymium borate · Crystal structure · Vibrational property · Optical property · Thermal stability

1 Introduction

Inorganic rare-earth borates have received intensive interests owing to their wide range of applications in nonlinear optics (NLO), laser hosts and photoluminescence materials [1–3]. Among the most attractive features of borate crystals, the key characteristics are their transparency in the wide range from mid-infrared to deep-ultraviolet [4], high optical damage threshold [5] and suitable physico-chemical stability [6]. Hitherto, $Na_3La_9O_3(BO_3)_8$ [7], $La_2CaB_{10}O_{19}$ [8], and $YAl_3(BO_3)_4$ [9] have been widely used as NLO crystals for second harmonic generation (SHG). Since the ionic radii of the rare-earth elements are close to each other, these rare-earth borates are favorable to host optical active cations such as Ce^{3+}, Nd^{3+} and Yb^{3+} [10]. Therefore, the rare-earth borates can further serve as an array of functional materials in optics: Ce^{3+}:$Li_6Y(BO_3)_3$ [11] as scintillator materials for neutron detection, Nd^{3+}:$YAl_3(BO_3)_4$ [12] as crystals for green laser emission, and Yb^{3+}:$LiGd_6O_5(BO_3)_3$ [13] as ultrashort-pulse lasers. Rare-earth orthoborate YBO_3 doped with Eu^{3+} and Tb^{3+} [14] are appropriate phosphors in plasma-display panels due to their high luminous efficacy and thermally stable luminescence yield.

✉ M. Mangir Murshed, murshed@uni-bremen.de | [1]University of Bremen, Institute of Inorganic Chemistry and Crystallography, Leobener Straße 7, 28359 Bremen, Germany. [2]University of Bremen, MAPEX Center for Materials and Processes, Bibliothekstraße 1, 28359 Bremen, Germany.

Recently, Pr^{3+} cation-doping materials have drawn an intense research attention due to their promising applications in white-light emitting diodes [15–17]. The Pr^{3+} cation is able to release rich fluorescence spectral lines in the red, orange, green, and blue regions, which originate from the electronic transition between the $4f$ inner-shell configurations. For instance, in the alkali-metal borates steady and high-efficiency red emission have been detected in Pr^{3+}:$KSr_4(BO_3)_3$ powder [18], Pr^{3+}:$Na_3La_9O_3(BO_3)_8$ crystal [19] and Pr^{3+} doped lithium borate glasses [20] when activated by blue or ultraviolet light due to $^3P_0 \rightarrow {}^3H_6$ and $^1D_2 \rightarrow {}^3H_4$ transitions. Despite much works on Pr^{3+}-doped borates, purely praseodymium borates have not been extensively studied. In search of novel rare-earth borate compounds the present investigation focus on A_2O–Pr_2O_3–B_2O_3 (A = alkali metal) quasi-ternary systems and their crystal-, chemico-physical properties. To the best of our knowledge, only $Li_3Pr_2(BO_3)_3$ [21], $LiPr_6O_5(BO_3)_3$ [22], $Na_3Pr(BO_3)_2$ [23] and $K_9Li_3Pr_3(BO_3)_7$ [24] were reported in these ternary systems. The alkali-metal praseodymium borate $K_2Pr_2O(BO_3)_2$ has been found to be a new member of the $K_2La_2(BO_3)_2O$ family [25]. The report particularly emphasizes on the synthesis, crystal structure, vibrational, optical and thermal properties of $K_2Pr_2O(BO_3)_2$.

2 Experimental

2.1 Synthesis

Single crystals of $K_2Pr_2O(BO_3)_2$ were obtained by means of the flux-assisted solid state reaction method. The starting materials K_2CO_3, PrO_2 and H_3BO_3 with a molar ratio of 1.5: 2: 3, respectively, were thoroughly ground in an agate mortar, and put into a platinum crucible. The mixture of the starting chemicals can be regarded as the target product $K_2Pr_2O(BO_3)_2$ together with the assisted-flux KBO_2 in the molar ratio of 1:1. The crucible was heated up to 1173 K in a muffle furnace with a heating rate of 100 K/h and maintained at that temperature for 12 h. Afterward, the crucible was cooled down to room temperature with a cooling rate of 300 K/h. The obtained greenish single crystals are found to be chunk-shaped with a dimension of tens of micrometer.

The polycrystalline samples of $K_2Pr_2O(BO_3)_2$ were prepared using a solid-state synthesis method in a platinum crucible. First, a stoichiometric batch of intimately mixed K_2CO_3, PrO_2 and H_3BO_3 (analytical grade) was heated at 773 K for 12 h to completely decompose K_2CO_3 and H_3BO_3. The resulting samples were then ground in agate mortar and heated further at 1123 K for 48 h. A 10% excess molar ratio of K_2CO_3 was added into the samples during the sintering process to compensate the evaporation of

potassium. The mixtures were repeatedly heated at 1123 K with intermediate grindings until their powder X-ray diffraction pattern confirms a pure phase.

2.2 X-ray single crystal diffraction

The small crystals of $K_2Pr_2O(BO_3)_2$ were isolated by mechanical fragmentation and picked using a polarization microscope. Single-crystal diffraction data were collected on a Bruker D8-Venture diffractometer in Kappa geometry with $Mo_{k\overline{\alpha}}$ radiation ($\lambda_{k\overline{\alpha}} = 71.0747(6)$ pm) at 297(2) K. A numerical absorption correction was applied to the intensity data sets. The systematic extinctions and $|E^2 - 1|$ statistics suggested the monoclinic space group $P2_1/c$; therefore the structure determination of $K_2Pr_2O(BO_3)_2$ was performed in this space group. The structure was finely solved via the intrinsic phasing method and successfully refined on F^2 by full-matrix least-square methods with the ShelxT and Shelxle program packages [26, 27]. All atoms were refined with anisotropic displacement parameters and the final difference Fourier synthesis did not reveal any significant residual electron density. All relevant details of the data collection and the refinement are listed in Table 1, atomic coordinates and displacement parameters in Table 2 and the bond valence sums (BVSs) in Table 3.

Further details of the crystal structure information can be obtained from FIZ Karlsruhe, 76,344 Eggenstein Leopoldshafen, Germany (fax: +49-7247-808-666; e-mail: crysdata@fiz-karlsruhe.de) on quoting the deposition number CSD-1978814.

2.3 X-ray powder diffraction

The powder X-ray diffraction (PXRD) pattern was recorded on a Panalytical X'Pert Pro powder diffractometer using Bragg–Brentano geometry with $CuK_{\alpha1,2}$ ($\lambda_{k\alpha1} = 154.05929(5)$ pm, $\lambda_{k\alpha2} = 154.4414(2)$ pm) radiation. The measurement was carried out at ambient condition in a range between 5° and 130° 2θ with a step size of 0.0167° and a data collection time of 30 s/step. The fundamental parameter approach, where the fundamental parameters were fitted against a LaB_6 standard material, was applied for the Rietveld refinement using "Diffrac^{Plus} Topas 6" software (Bruker AXS GmbH, Karlsruhe, Germany). The starting lattice parameters and atomic coordinates were taken from the results of the single crystal structure determination. The average crystallite size was calculated from all observed X-ray reflections, which is described as $L_{Vol}(IB)$ by the TOPAS suite. Of notes, $L_{Vol}(IB)$ refers to the volume-weighted mean of the coherently diffracted domain size using the integral breadth for the description of the reflection profile.

Table 1 Crystal structure determination of $K_2Pr_2O(BO_3)_2$ in the space group $P2_1/c$ (No. 14) from single crystal and powder X-ray diffraction data

Crystals	Single	Powder
Dimension $(\mu m^3)/L_{Vol}(IB)$ (nm)	$93 \times 66 \times 52$	249(8)
a (pm)	1133.77(3)	1135.00(3)
b (pm)	660.47(2)	660.64(2)
c (pm)	1071.30(3)	1072.03(3)
β (°)	117.07(1)	117.13(1)
Z	4	4
Temperature (K)	297(2)	300(2)
Diffractometer	Bruker D8 Venture	Panalytical X'Pert Pro
Wavelength (pm)	71.0747(6)	154.1866(1)
Absorption coefficient (mm^{-1})	14.638	113.568(6)
Absorption correction method	Numerical	
$F(000)/e^-$	888	888
$\theta/2\theta$ range (°)	2.017–46.021	5–130
Range in hkl	$-22 \leq h \leq 20,$	$0 \leq h \leq 13,$
	$-12 \leq k \leq 13,$	$0 \leq k \leq 7$
	$-20 \leq l \leq 21$	$0 \leq l \leq 11$
Reflections collected	64145	1230
Data/restraints/parameters	6129/0/119	7480/8/54
Goodness-of-fit on F^2	1.043	1.92
R_1/wR_2 [I > 2σ(I)]	0.0318/0.0566	$R_p = 0.0588$
R_1/wR_2 (all data)	0.0401/0.0438	$R_{wp} = 0.07786$

2.4 UV/Vis spectroscopy

The UV/Vis diffuse reflectance measurement was collected from 200 to 850 nm with a step of 1 nm on a UV-2700 spectrophotometer (Shimadzu, Japan) equipped with an ISR-2600 plus two-detector integrating sphere (Pike Technologies, USA). The baseline correction was carried out against $BaSO_4$ powder.

2.5 Vibration spectroscopy

The Fourier transform infrared (FTIR) spectrum was recorded on a Bruker IFS66v/S spectrometer using the standard KBr method between 370 and 4000 cm^{-1}. KBr pallets consist of 2 mg sample mixed with 200 mg KBr (sample) and 200 mg KBr (reference), pressed at 100 kN, forming disks of 12 mm in diameter.

Due to laser induced susceptibility of the $4f$-electronic transitions the Raman spectra were measured at ambient condition using at least three lasers (532 nm, 633 nm and 785 nm), and found that the band numbers and the respective frequency positions are laser-independent. To avoid the absorption areas (see UV–Vis reflectance spectrum below), the 785 nm laser was chosen for better spectral resolution. Temperature-dependent Raman spectra were recorded on a LabRam ARAMIS (Horiba Jobin Yvon) Micro-Raman spectrometer equipped with a laser working at 785 nm and less than 5 mW power on the sample surface. The use of a $50 \times$ long working distance objective (Olympus) with a numerical aperture of 0.55 provides a focus spot of about 2 µm diameter when closing the confocal hole to 200 µm. Raman spectra were collected in the range 85–1700 cm^{-1} with a spectral resolution of approximately 1.1 cm^{-1} using a moving grating of 1800 grooves/mm and a thermoelectrically cooled CCD detector (Synapse, 1024×256 pixels). The spectral positions were calibrated against the Raman mode of Si before and after the sample measurements. The position of the Si peak was repeatedly measured against the Rayleigh line (0.0 cm^{-1}) yielding a value of 520.7 ± 0.1 cm^{-1}. The linearity of the spectrometer was calibrated against the emission lines of a neon lamp. For the low-temperature measurements, a pressed pellet of powder sample was placed on a Linkam cooling stage (THMS600) attached to a pump (LNP95 Cooling Pump) that provides a continuous flow of liquid nitrogen. The measurements were carried out between 78 and 300 K. A ramp rate of 5 K/min and a holding time of 5 min were followed to properly equilibrate the temperature. For the spectrum at ambient condition the baseline was linearly corrected, bands were fitted with Pseudo-Voigt lineshape.

2.6 Thermal analysis

Simultaneous thermogravimetric analysis/differential scanning calorimetry (TGA/DSC) measurements were

Table 2 Crystal structural data of $K_2Pr_2O(BO_3)_2$

Atom	Wyckoff	SOF	x	y	z	U_{eq}	B_{iso}
Pr1	4e	1	0.51850(2)	0.04466(2)	0.31939(2)	49.0(2)	–
			0.5184(3)	*0.0452(4)*	*0.3202(3)*	–	*0.46(5)[a]*
Pr2	4e	1	0.32360(2)	0.41647(2)	0.41561(2)	56.3(2)	–
			0.3230(3)	*0.4159(4)*	*0.4162(3)*	–	*0.46(5)[a]*
K1	4e	1	0.03193(5)	0.06011(7)	0.26414(5)	129.9(8)	–
			0.0320(9)	*0.0569(15)*	*0.2666(10)*	–	*0.55(18)[b]*
K2	4e	1	0.11866(5)	0.74422(8)	0.05575(5)	137.7(3)	–
			0.1200(9)	*0.7564(15)*	*0.0596(12)*	–	*0.55(18)[b]*
B1	4e	1	0.6946(2)	0.3446(3)	0.1441(2)	67(3)	–
			0.6946[d]	*0.3446[d]*	*0.1441[d]*	–	*0.529[d]*
B2	4e	1	0.1978(2)	0.2469(3)	0.0897(2)	73(3)	–
			0.1978[d]	*0.2469[d]*	*0.0897[d]*	–	*0.576[d]*
O1	4e	1	0.79983(15)	0.2513(2)	0.14046(17)	103(3)	–
			0.808(3)	*0.258(5)*	*0.144(3)*	–	*1.5(3)[c]*
O2	4e	1	0.12430(16)	0.3490(3)	0.46490(17)	114(3)	
			0.128(3)	*0.327(4)*	*0.482(3)*		*1.5(3)[c]*
O3	4e	1	0.14560(16)	0.3469(3)	0.16568(17)	119(3)	–
			0.154(2)	*0.363(4)*	*0.169(3)*	–	*1.5(3)[c]*
O4	4e	1	0.63161(15)	0.2468(2)	0.21263(17)	90(3)	–
			0.622(3)	*0.267(4)*	*0.221(3)*	–	*1.5(3)[c]*
O5	4e	1	0.52705(15)	0.3776(2)	0.40277(16)	77(2)	–
			0.528(3)	*0.395(4)*	*0.419(3)*	–	*1.5(3)[c]*
O6	4e	1	0.33651(15)	0.2428(2)	0.13950(17)	97(3)	–
			0.346(3)	*0.233(4)*	*0.142(3)*	–	*1.5(3)[c]*
O7	4e	1	0.35215(16)	0.0341(2)	0.41402(17)	92(3)	–
			0.361(2)	*0.010(4)*	*0.402(3)*	–	*1.5(3)[c]*

The isotropic ($B_{iso}/10^4 \times pm^2$) and equivalent isotropic (U_{eq}/pm^2) atomic displacement parameters are obtained from powder X-ray and single crystal X-ray diffraction data analysis, respectively

[a,b,c] Values with the same letters were constrained to each other during the refinements

[d] These values were fixed during the refinement. U_{ij} tensors can be obtained from CSD-1978814

performed on TGA/DSC 3[+] STAR[e] system of Mettler Toledo. The sample was measured with a heating rate of 10 K/min and a continuous N_2 flow of 20 mL/min from 300 to 1473 K. Afterward, the data were normalized to their respective mass. Approximately 16.159 mg of $K_2Pr_2O(BO_3)_2$ was measured relative to an empty corundum crucible as the reference. A drift correction was applied based on empty crucible data.

3 Results and discussion

3.1 Crystal structure of $K_2Pr_2O(BO_3)_2$

$K_2Pr_2O(BO_3)_2$ crystallizes in a new structure type in the monoclinic space group $P2_1/c$ (no. 14) with lattice parameters of $a = 1133.77(3)$ pm, $b = 660.47(2)$ pm, $c = 1071.30(3)$ pm, $\beta = 117.072(1)°$, and $Z = 4$. The structural building units of $K_2Pr_2O(BO_3)_2$, as shown in Fig. 1, can be regarded as PrO_8

dodecahedra, KO_6 octahedra and KO_7 pentagonal bipyramid together with isolated trigonal planar BO_3 groups. Both Pr(1) and Pr(2) form distorted PrO_8 dodecahedra, where the Pr–O bond lengths vary from 235.9(2) pm to 260.1(2) pm in $Pr(1)O_8$, and from 234.6(2) to 274.6(2) pm in $Pr(2)O_8$. The $Pr(1)O_8$ dodecahedra are axially connected with its neighbors via sharing two triangular faces to construct an infinite zig-zag chain along the b-axis (Fig. 1b). These zig-zag chains are further joined together by edge-sharing to form infinite two dimensional $Pr(1)O_{(3+3+2)/2}$ layers with elongated hexagonal voids in the bc-plane. Such a 2D REO_n layer with "honeycomb-like" voids was also found in other rare-earth borates, for instance, in $Na_3La_2(BO_3)_3$ [28]. By contrast, two $Pr(2)O_8$ dodecahedra share their O(5)-O(5) edge to construct $Pr(2)_2O_{14}$ dimers that fill into those "honeycomb-like" voids (Fig. 1c). It is interesting to mention that O(5), the isolated oxygen anion in $K_2Pr_2O(BO_3)_2$, connects only to Pr-atoms and plays an important role in the formation of a $Pr(2)_2O_{14}$ dimer.

Table 3 Interatomic bond distance/pm and bond valence (BV/v.u.) and bond valence sum (BVS/v.u.) of the PrO_8, $KO_{6,7}$ and BO_3 polyhedra in $K_2Pr_2O(BO_3)_2$

Bond	Bond length	BV	Bond	Bond length	BV
$Pr1O_8$			$Pr2O_8$		
Pr1–O5	235.9(2)	0.551(2)	Pr2–O5	234.6(2)	0.570(2)
Pr1–O5	245.6(2)	0.424(2)	Pr2–O5	238.6(2)	0.511(3)
Pr1–O6	246.3(2)	0.416(1)	Pr2–O1	253.9(2)	0.339(1)
Pr1–O4	246.4(2)	0.415(2)	Pr2–O7	254.7(2)	0.331(1)
Pr1–O6	249.3(2)	0.384(2)	Pr2–O3	255.6(2)	0.323(1)
Pr1–O7	251.6(2)	0.360(2)	Pr2–O6	256.2(2)	0.318(2)
Pr1–O4	252.0(2)	0.356(1)	Pr2–O2	258.25(2)	0.301(2)
Pr1–O7	260.1(2)	0.286(1)	Pr2–O4	274.6(2)	0.193(1)
	BVS(Pr1)	3.190(5)		BVS(Pr2)	2.886(5)
$K1O_6$			$K2O_7$		
K1–O1	265.9(2)	0.241(1)	K2–O1	265.4(2)	0.244(1)
K1–O1	266.5(2)	0.237(1)	K2–O2	275.0 (2)	0.188(1)
K1–O2	267.3(2)	0.232(1)	K2–O4	278.91(2)	0.169(1)
K1–O2	270.4(2)	0.213(1)	K2–O3	283.51(2)	0.149(1)
K1–O3	275.7(2)	0.185(1)	K2–O2	286.8(2)	0.137(1)
K1–O3	282.4(2)	0.154(1)	K2–O3	291.5(2)	0.121(0)
			K2–O1	295.1(2)	0.109(1)
	BVS(K1)	1.261(1)		BVS(K2)	1.118(1)
$B1O_3$			$B2O_3$		
B1–O1	135.9(3)	1.033(8)	B2–O2	136.7(3)	1.011(7)
B1–O7	139.1(3)	0.948(6)	B2–O3	137.3(3)	0.992(9)
B1–O4	139.3(3)	0.939(8)	B2–O6	141.3(3)	0.894(7)
	BVS(B1)	2.920(13)		BVS(B2)	2.897(13)

Therefore, $[Pr_2O(BO_3)_2]^{2-}$ sheets are composed of $Pr(1)O_{(3+3+2)/2}$ layers, $Pr(2)_2O_{14}$ dimers, isolated $B(1)O_3$ and $B(2)O_3$ planar groups via corner and edge sharing in the ac-plane. Two adjacent $[Pr_2O(BO_3)_2]^{2-}$ sheets in the structure are regulated by the inversion center (Fig. 1d). Two types of potassium K(1) and K(2) are found to occupy the inter-sheet space and separate the $[Pr_2O(BO_3)_2]^{2-}$ sheets along the a-axis. Similar stacking modes were also observed in other layered alkali-metal rare-earth borates such as $K_9Li_3Nd_3(BO_3)_9$ [24] and $Rb_2LiNd(BO_3)_2$ [24]. K(1) is six-fold coordinated to form a distorted $K(1)O_6$ octahedron while K(2) connects to seven oxygens in exhibition of a distorted pentagonal bipyramid $K(2)O_7$. The K–O distances range from 265.9(2) to 282.4(2) pm with mean values of 273.6(2) pm and 282.3(2) pm for $K(1)O_6$ and $K(2)O_7$ polyhedra, respectively. These values fit well with the sum of the ionic radii of oxygen and potassium in sixfold and sevenfold coordination [29]. In the unit cell, both B(1) and B(2) atoms are three-coordinated to oxygen atoms, forming isolated planar BO_3 groups. The B-O distances range from 134.2(5) to 141.0(6) pm with an averaged bond length of 137.0(3) pm for $B(1)O_3$ and 137.9(3) pm for $B(2)O_3$, respectively.

These values are in agreement with those of other alkali-metal rare-earth borate-containing isolated BO_3 groups, for instance 137.1 pm in $K_3Sm(BO_3)_2$ [30], 137.4 pm in $Li_3K_3Y_7(BO_3)_9$ [31] and 137.6 pm in $K_9Li_3Nd_3(BO_3)_7$ [24]. The bond valence sums (BVS) calculation was performed for $K_2Pr_2O(BO_3)_2$ using the Bondstr software of the FullProf suite [32], which are listed in Table 3. The structural BVSs of the atoms correspond well with the formal integer charge of the respective atoms. To confirm the single crystal structure of its bulk representative as well the purity of the as-synthesized $K_2Pr_2O(BO_3)_2$ polycrystalline powder sample, X-ray powder data Rietveld refinements were performed. The corresponding Rietveld plot is shown in Fig. 2. The metric parameters ($a = 1135.00(3)$ pm, $b = 660.641(15)$ pm, $c = 1072.03(3)$ pm, $\beta = 117.128(2)°$ and $V = 715.41(3) \times 10^6$ pm^3) are in excellent agreement with those obtained from the single crystal structure determination (Tables 1, 2).

3.2 UV/Vis spectrum

The UV/Vis reflectance spectrum of $K_2Pr_2O(BO_3)_2$ in the range of 200–850 nm is shown in Fig. 3. The optical absorption in the visible range accounts for the green color of $K_2Pr_2O(BO_3)_2$ and also corresponds well to the presence of Pr^{3+} cation. All visible absorption bands in $K_2Pr_2O(BO_3)_2$ result from the inner-shell $4f^2$-configuration electronic transitions from the ground state ($^3H_4$) to various excited states. According to the energy level scheme proposed by Dieke and Crosswhite [33], these bands from 400 to 520 nm can be assigned, respectively to $^3H_4 \rightarrow {}^3P_2,\ {}^3P_1,$ and $^3P_0$, while the band in the range of 550–650 nm ascribed to $^3H_4 \rightarrow {}^1D_2$. Of particular notes, we clearly observe the Stark splitting of $^3P_2,\ {}^3P_1,$ and $^3P_0$ and $^1D_2$ multiplets, which may help calculate the crystal field levels of Pr^{3+} cation in $K_2Pr_2O(BO_3)_2$. The monotonic drop of the reflectance between 290 and 270 nm (Fig. 3) corresponds to the valence-to-conduction-band absorption edge. The Kubelka–Munk function [34] treatment followed by the Tauc method [35] are often used to estimate the corresponding bandgap energy by finding the intercept of the abscissa from the following relations:

$$F(R) = \frac{(1-R)^2}{2R}$$
$$F(R)(h\nu) = B(h\nu - E_g)^n$$

where R is the reflectance [%] in the UV/Vis spectra, h the Planck's constant, ν the frequency of light, E_g the bandgap in eV, and n-the type of optical transition. That is, $n = 2$ for an indirect transition (plotted as $[F(R)\cdot(h\nu)]^{1/2}$ vs. $h\nu$) and $n = 1/2$ for a direct transition (plotted as $[F(R)\cdot(h\nu)]^2$ vs. $h\nu$). The intercepts of the abscissa (Fig. 3) demonstrates bandgap values of 4.40(1) eV and 4.50(1) eV for an indirect and
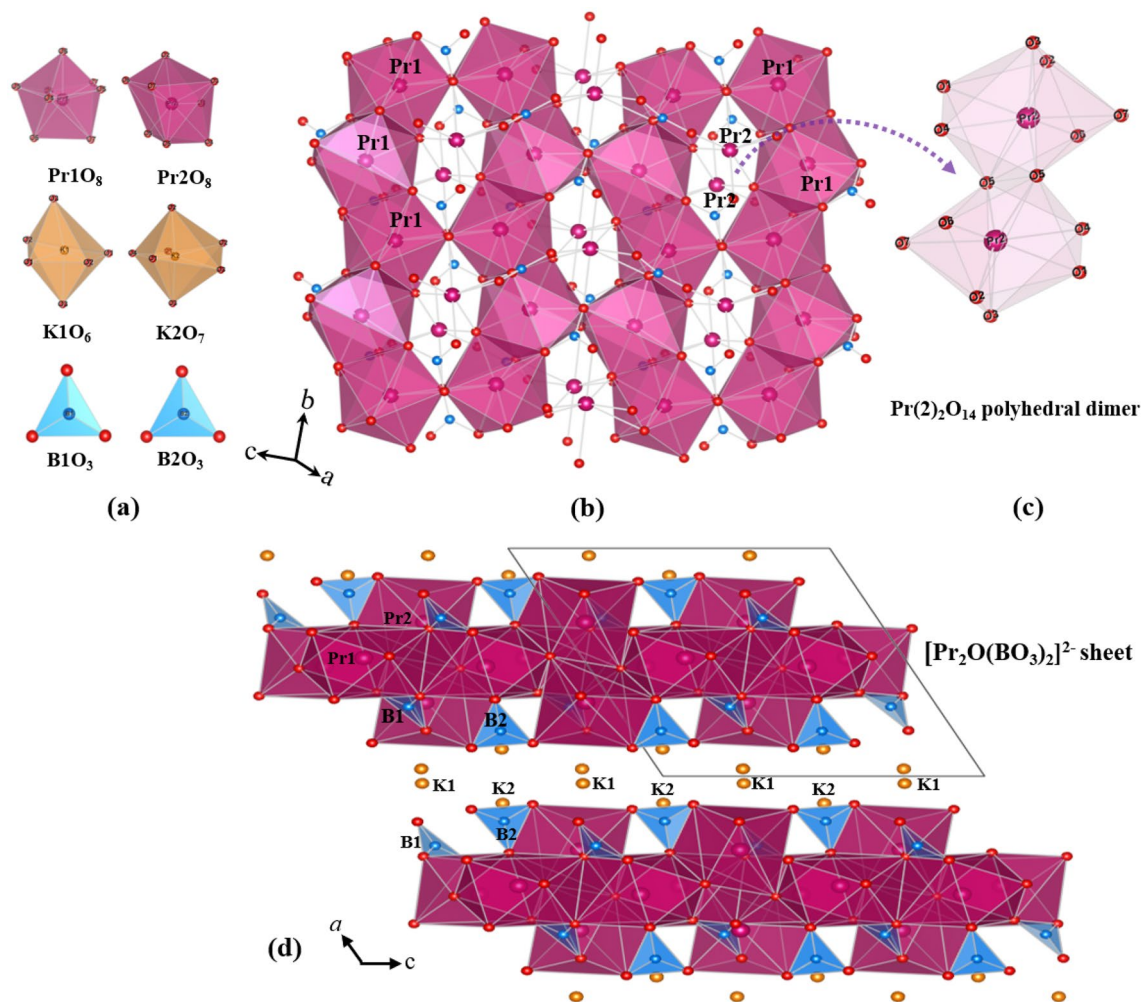
Fig. 1 Crystal structure of $K_2Pr_2O(BO_3)_2$, showing polyhedral structural units (**a**) connectivity of Pr(1)O_8 dodecahedra (**b**), Pr(2)$_2O_{14}$ polyhedral dimer (**c**), and view of the structure of $K_2Pr_2O(BO_3)_2$ along the *b*-axis (**d**)

direct transition, respectively. These bandgap values of $K_2Pr_2O(BO_3)_2$ are smaller than those of 4.96 eV for λ-$PrBO_3$ [36] and 6.32 eV for $Rb_2LiLaB_2O_6$ [37]. Recently, the derivation of absorption spectrum fitting (DASF) method was proposed by Souri et al. [38] for thin films to calculate the bandgap energies without any presumption of the nature of the transition. Notably, the DASF method can also be expressed as follows proposed by Kirsch et al. [39, 40] for powder samples:

$$\frac{d\ln F(R)}{dh\nu} = \frac{n}{h\nu - Eg}$$

The obtained bandgap of 4.49(1) eV using the DASF method is similar to the determined bandgap of 4.50(1) eV for a direct transition within the estimated

uncertainty. Therefore, the combined approach suggests a direct bandgap transition for $K_2Pr_2O(BO_3)_2$.

3.3 FTIR and Raman spectra

The observed FTIR and Raman spectra along with the fitted compound and component models are shown in Fig. 4. Since the crystal structure of $K_2Pr_2O(BO_3)_2$ adopts $P2_1/c$ space group, factor group analysis predicts 156 vibrational modes at the zone center ($39A_g + 39A_u + 39B_g + 39B_u$), where 75 modes ($38A_u + 37B_u$) are IR active, 78 modes ($39A_g + 39B_g$) are Raman active and 3 are acoustic modes ($A_u + 2B_u$). To fit the observed IR spectrum, it requires 41 bands. The bands between 400 and 550 cm^{-1} can be attributed to bending of Pr–O, which was explicitly characterized in other praseodymium oxides [41, 42] The bands
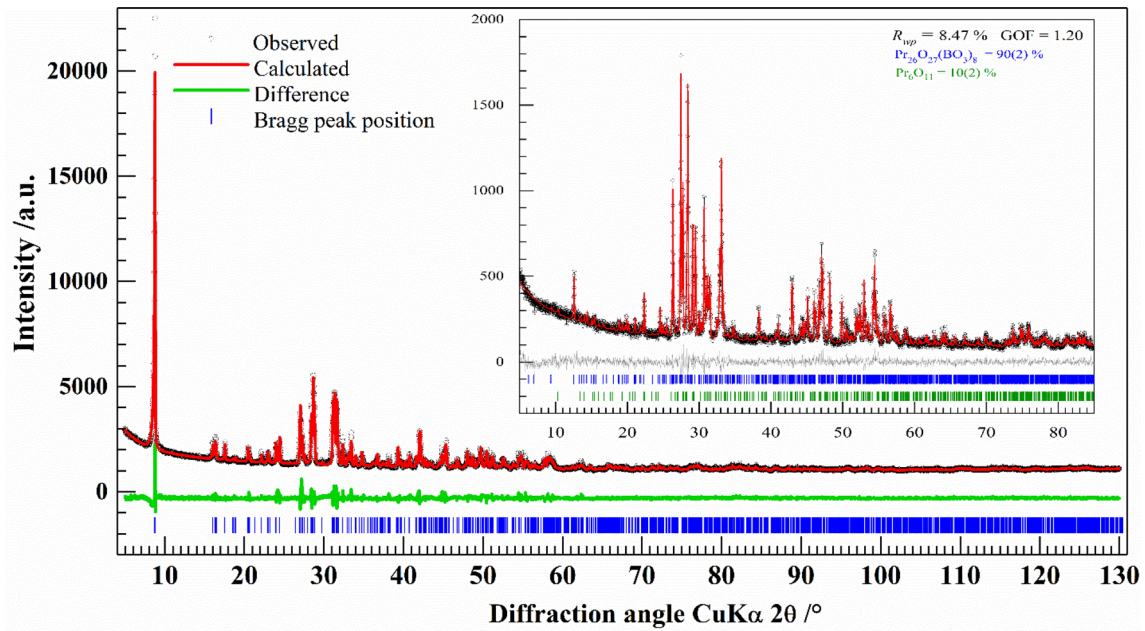
Fig. 2 X-ray powder data Rietveld plots of $K_2Pr_2O(BO_3)_2$ and of the decomposition products as inset
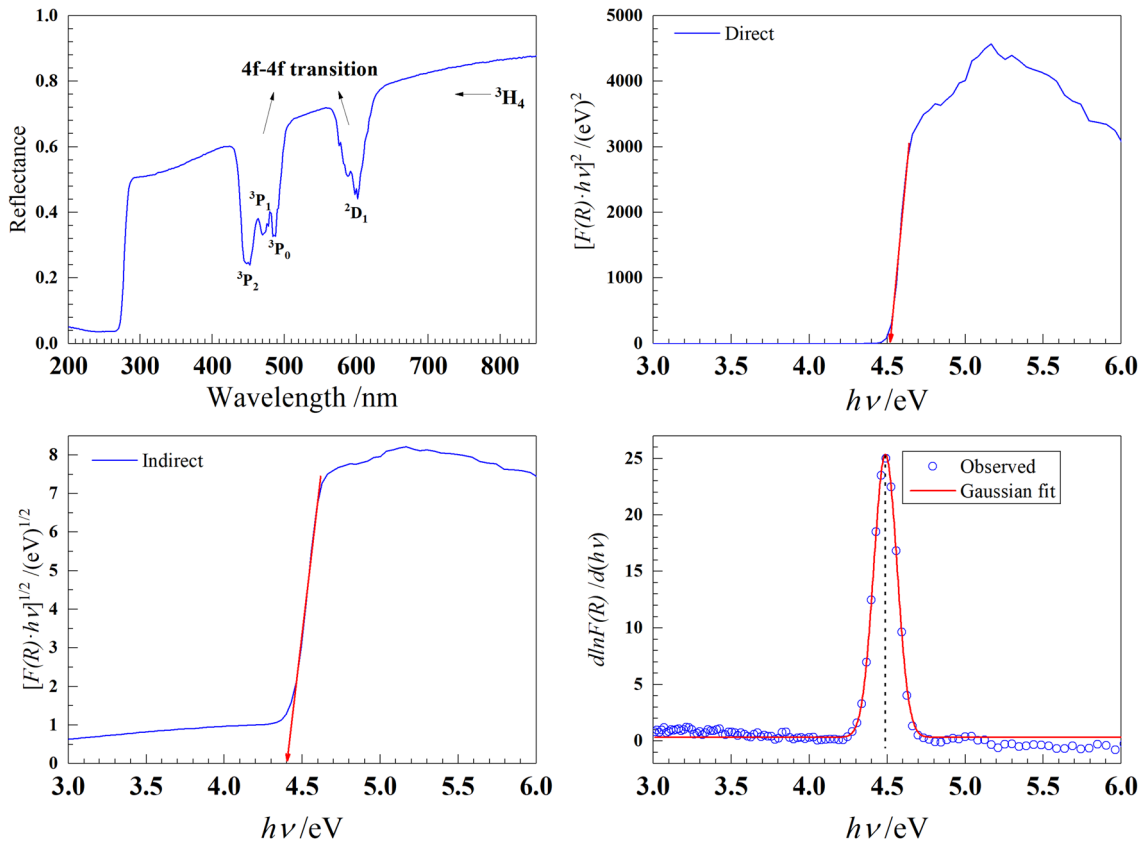

Fig. 3 Reflectance spectrum of $K_2Pr_2O(BO_3)_2$ (top left), Tauc plots for indirect (bottom left) and direct (top right) optical transitions, and DASF plot (bottom right)
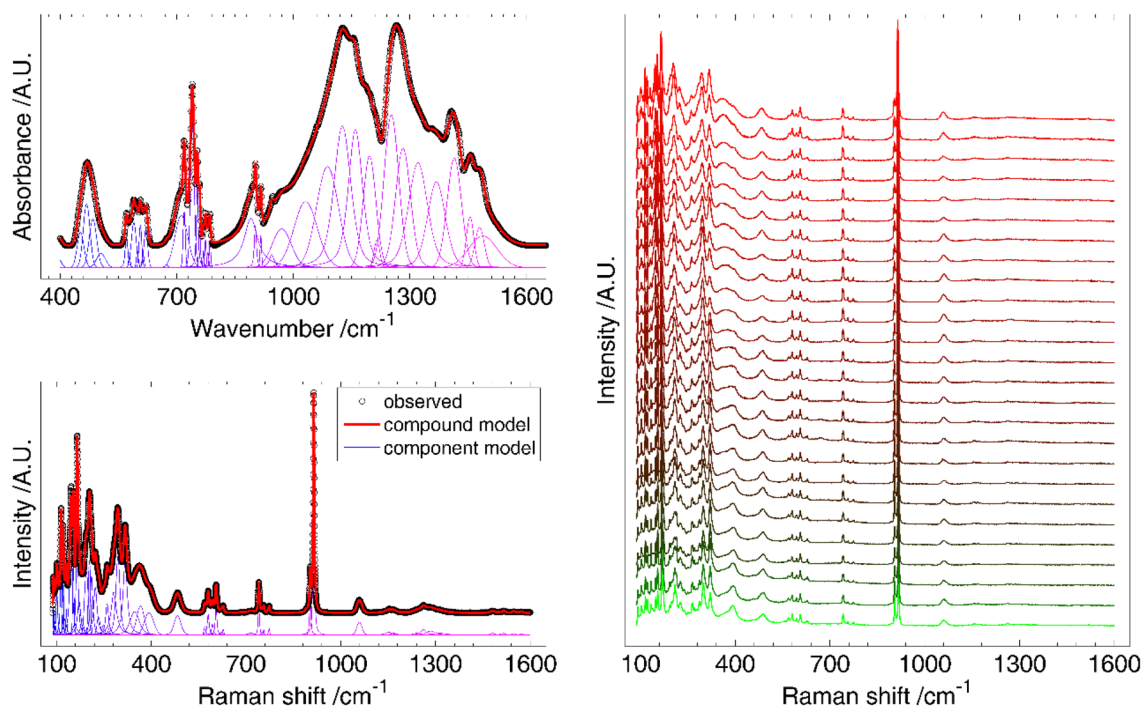
Fig. 4 FTIR (left top) and Raman (left bottom) spectra of $K_2Pr_2O(BO_3)_2$ at ambient condition along with fitted compound and component models. Temperature-dependent Raman spectra (right); temperature increases upward from 78 to 300 K

between 600 and 1600 cm^{-1} owing to vibration of planar BO_3^{3-} groups, can be categorized into four different types [37, 43, 44]: the in-plane bending (v4; 550–700 cm^{-1}), out-of-plane bending (v2; 740–780 cm^{-1}) of BO_3, B–O symmetric stretching (v1; ~903 cm^{-1}) and B–O asymmetric stretching (v3; 1000 cm^{-1} and 1500 cm^{-1}). Clearly, the v2 and v3 modes have much stronger absorption than that of v3 and v1. Group analysis of an ideal planar BO_3 group possesses D_{3h} symmetry, where v2 and v3 are IR active, whereas the v1 is IR inactive. The clear appearance of v1 in the IR spectrum indicates that the BO_3 groups in $K_2Pr_2O(BO_3)_2$ are distorted from an ideal symmetry.

The observed Raman spectrum of $K_2Pr_2O(BO_3)_2$ at ambient condition could be fitted with *56 component* peaks (Fig. 4). Several intense bands below 550 cm^{-1} can be ascribed to the bending and stretching vibrations of K–O and Pr–O bonds as well as the lattice vibrations. The bands observed in the range of 600–700 cm^{-1} and 700–800 cm^{-1} correspond to the v4 and v2 modes, respectively. The most intense bands occur at 915 cm^{-1} resulting from the v1 mode. The symmetric stretching mode (v1) of BO_3^{3-} group is a strong Raman active vibration as known from other Pr^{3+}-containing orthoborates such as λ-$PrBO_3$ [37, 43, 44] and $KCaPr(BO_3)_2$ [45]. Above 1000 cm^{-1}, one peak locating at 1050 cm^{-1} and several border bands are found and can be ascribed to the v3 mode of BO_3^{3-} groups. Of notes, the Raman spectrum also clearly confirms the vibrational

features of BO_3 and PrO_x groups in $K_2Pr_2O(BO_3)_2$. The temperature-dependent Raman spectra of $K_2Pr_2O(BO_3)_2$ from 78 to 300 K (Fig. 4) show that the overall global quasi-harmonic change is not significant within the investigated low-temperature range. For instance, the intense band at 916.2(1) cm^{-1} at 78 K shifts only to 914.6(1) cm^{-1} at 300 K. Any phase transition driven by any optical soft-mode was not observed during the sample cooling from 300 to 78 K. Extrapolation of the frequency of this mode down to 0 K suggests that the compound $K_2Pr_2O(BO_3)_2$ would be stable, a guideline for the phonon calculation using density functional theory calculation.

3.4 Thermal analysis

For the bulk single-crystal growth of inorganic compounds, determination of the melting point or the decomposition temperature is indispensable. The thermal behavior of $K_2Pr_2O(BO_3)_2$ was investigated by using simultaneous TGA and DSC methods. As shown in Fig. 5, the DSC curve demonstrates one sharp endothermic signal peak at 1318(1) K as well as one border and tiny peaks after 1400 K. The distinct endotherm in the range of 1273(3) K and 1330(3) K corresponds to melting or thermal decomposition. From the TG curve a weight-loss of 21.96(1)% is found to be at 1273(3) K. After the TGA /DSC experiment, X-ray powder data Rietveld refinement (inset Fig. 2)
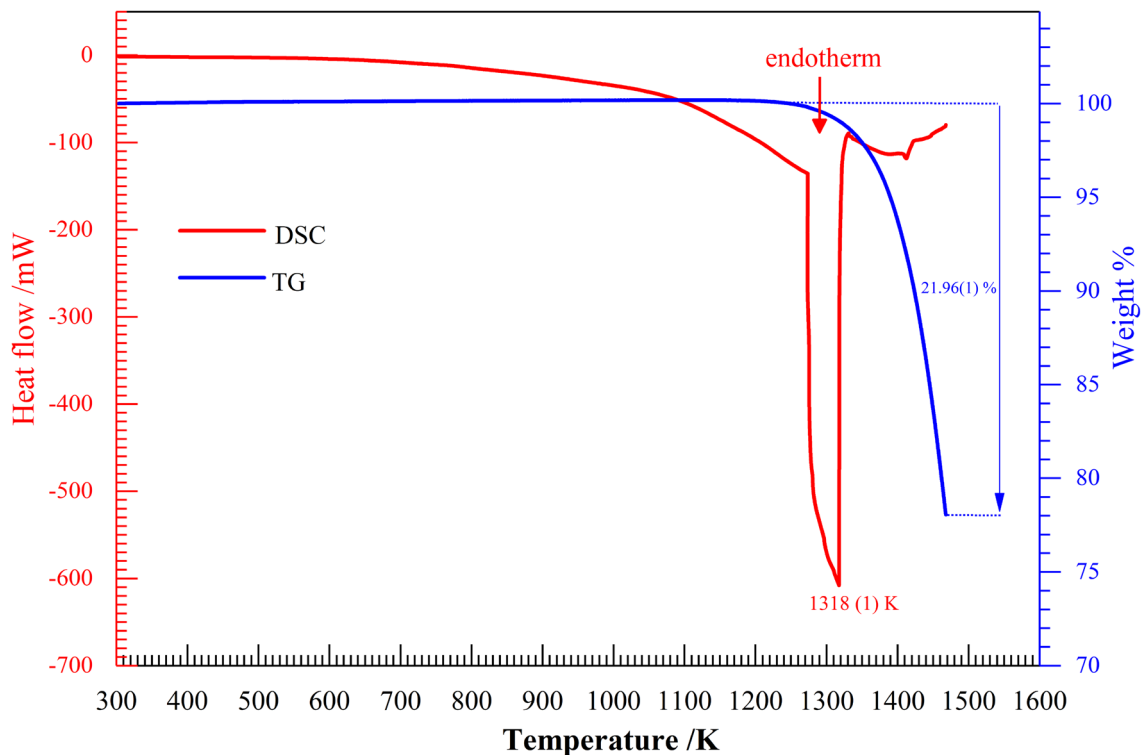
Fig. 5 Thermogravimetry (TG) and differential scanning calorimetry (DSC) curves of $K_2Pr_2O(BO_3)_2$

demonstrates that the residual consists of $Pr_{26}O_{27}(BO_3)_8$ and Pr_6O_{11} phases. It is worthwhile to note that we used $Nd_{26}O_{27}(BO_3)_8$ [46] as the starting model and replaced Nd -atom with Pr-atom in the same Wyckoff position during the Rietveld refinement. For the obtained isotypic $Pr_{26}O_{27}(BO_3)_8$ lattice parameters of $a = 676.160(17)$ pm, $b = 1269.56(4)$ pm, $c = 1432.28(3)$ pm, $a = 89.9979(17)°$, $β = 99.9008(17)°$, $γ = 89.9995(19)°$ were calculated. From the distinct weight loss during the heating process one can safely assume that $K_2Pr_2O(BO_3)_2$ decomposes into $Pr_{26}O_{27}(BO_3)_8$, Pr_6O_{11} and potassium borates which eventually evaporates at the high-temperature regime. The TGA /DSC also confirms that $K_2Pr_2O(BO_3)_2$ possess an incongruent melting point, suggesting that the flux method would be necessary for the growth of its bulk crystal.

4 Conclusion

The detailed structural, spectroscopic and thermal analysis reveal that the synthesized alkali metal praseodymium borate $K_2Pr_2O(BO_3)_2$ belongs to the new member of the $K_2La_2(BO_3)_2O$ family [25] providing also a new structure type. The crystal structure consists of 2D $[Pr_2O(BO_3)_2]^{2-}$ sheets and K^+ cations in a layered

stacking along the a-axis. The greenish color stems from the electronic transitions from the ground state to various excited states within the $4f^2$-configuration rather than from the fundamental absorption edge that lies in the UV-region. Since Pr^{3+} cation is of interest due to its photoluminescence property, $K_2Pr_2O(BO_3)_2$ may be a prospective red phosphor under the radiation of blue light [15–17]. Density functional theory (DFT) calculation would be necessary to distinguish the observed Raman and infrared bands between phonon at the zone-center and photoluminescence as well as for a fuller assignment of the modes. However, the $4f$-electrons of the rare-earth elements are over delocalized, sometimes leading to unrealistic/unphysical potentials and may provide inaccurate phonon calculations. Therefore, additional cares must be taken of in calculating the phonon spectra of the compound, which may be computationally very expensive. Given that $K_2Pr_2O(BO_3)_2$ is an incongruent melting compound, the bulk crystals may be grown via high-temperature flux method, which would help elucidate possible anisotropic properties.

Compliance with ethical standards

Conflict of interest The authors declare that they have no conflict of interest.

References

1. Mutailipu M, Xie Z, Su X, Zhang M, Wang Y, Yang Z, Janjua MRSA, Pan S (2017) Chemical cosubstitution-oriented design of rare-earth borates as potential ultraviolet nonlinear optical materials. J Am Chem Soc 139:18397–18405

2. Yoshida A, Schmidt A, Petrov V, Fiebig C, Erbert G, Liu J, Zhang H, Wang J, Griebner U (2011) Diode-pumped mode-locked Yb:YCOB laser generating 35 fs pulses. Opt Lett 36:4425–4427

3. Kruopyte A, Giraitis R, Juskenas R, Enseling D, Jüstel T, Katelnikovas A (2017) Luminescence and luminescence quenching of efficient GdB_5O_9: Eu^{3+} red phosphors. J Lumin 192:520–526

4. Yao W, He R, Wang X, Lin Z, Chen CJ (2014) Analysis of deep-UV nonlinear optical borates: approaching the end. Adv Opt Mater 2:411–417

5. Kumar RA, Arivanandhan M, Hayakawa Y (2013) Recent advances in rare earth-based borate single crystals: potential materials for nonlinear optical and laser applications. Prog Cryst Growth Charact Mater 59:113–132

6. Chen C, Sasaki T, Li R, Wu Y, Lin Z, Mori Y, Hu Z, Wang J, Aka G, Yoshimura M (2012) Nonlinear optical borate crystals: principals and applications. Wiley, Hoboken

7. Reshak AH, Auluck S, Kityk I (2008) Optical susceptibilities of $Na_3La_9O_3(BO_3)_8$, ternary oxyborate nonlinear single crystal: theory and experiment. J Phys Condens Matter 20:145209

8. Wang G, Lu J, Cui D, Xu Z, Wu Y, Fu P, Guan X, Chen C (2002) Efficient second harmonic generation in a new nonlinear $La_2CaB_{10}O_{19}$ crystal. Opt Commun 209:481–484

9. Rytz D, Gross A, Vernay S, Wesemann V (2008) $YAl_3(BO_3)_4$: a novel NLO crystal for frequency conversion to UV wavelengths. In: Proceedings of SPIE 6998, solid state lasers and amplifiers III, 2008, p 699814

10. Eichler HJ, Eichler J, Lux O (2018) Lasers: basics, advances and applications. Springer, Berlin

11. Yin J, Zhang J, Wang J, Du F, Li R, Pan S, Pan J (2018) Growth and scintillation properties of Ce: $Li_6Y(BO_3)_3$ crystal enriched with ^{10}B isotopes. Radiat Meas 113:20–24

12. Jaque D, Capmany J, García Solé J (1999) Red, green, and blue laser light from a single Nd: $YAl_3(BO_3)_4$ crystal based on laser oscillation at 1.3 μm. Appl Phys Lett 75:325–327

13. Jubera V, Veber P, Chavoutier M, Garcia A, Adamietz F, Rodriguez V, Chaminade J-P, Velázquez M (2010) Crystal growth and optical characterizations of Yb^{3+}-doped $LiGd_6O_5(BO_3)_3$ single crystal: a new promising laser material. CrystEngComm 12:355–357

14. Dexpert-Ghys J, Mauricot R, Caillier B, Guillot P, Beaudette T, Jia G, Tanner PA, Cheng B-M (2010) VUV excitation of YBO_3 and (Y, Gd)BO_3 phosphors doped with Eu^{3+} or Tb^{3+}: comparison of efficiencies and effect of site-selectivity. J Phys Chem C 114:6681–6689

15. Han B, Dai Y, Zhang J, Wang X, Shi W, Shi H (2018) $NaLaMgWO_6$:Pr^{3+}: a novel blue-light excitable red-emitting phosphor for white light-emitting diodes. J Lumin 196:275–280

16. Niu L, Zhou Y, Zhu C, He Z, Meng X (2019) Pr^{3+} doped oxyfluoride silicate glasses for LEDs. Ceram Int 45:4108–4112

17. Marek L, Sobczyk M (2018) Spectroscopic investigations of Pr^{3+} ions in Na_2O-La_2O_3-ZnO-TeO_2 glasses. J Non-Cryst Solids 487:96–103

18. Ma S-Z, Feng W-L, Chen R, Peng Z-Q (2017) $KSr_4(BO_3)_3$: Pr^{3+}: a new red-emitting phosphor for blue-pumped white light-emitting diodes. J Alloys Compd 700:49–53

19. Luo X, Shan F, Xu T, Zhang X, Zhang G, Wu Y (2016) Growth and optical properties of Pr3+ doped $Na_3La_9O_3(BO_3)_8$ crystal. J Cryst Growth 455:1–5

20. Ramteke D, Swart H, Gedam R (2016) Spectroscopic properties of Pr^{3+} ions embedded in lithium borate glasses. Phys B 480:111–115

21. Abdullaev G, Mamedov KS, Amiraslanov I, Magerramov A (1977) Crystal structure of lithium praseodymium orthoborate $Li_3Pr_2(BO_3)_3$. J Struct Chem 18:331–333

22. Chaminade J-P, Gravereau P, Jubera V, Fouassier C (1999) A new family of lithium rare-earth oxyborates, $LiLn_6O_5(BO_3)_3$ (Ln = Pr – Tm): crystal structure of the gadolinium phase $LiGd_6O_5(BO_3)_3$. J Solid State Chem 146:189–196

23. Wang Z, Li H, Cai G, Jin Z (2016) Synthesis, crystal structure, and thermal stability of new borates $Na_3REB_2O_6$ (RE = r, Sm, Eu). Powder Diffr 31:110–117

24. Chen P, Xia M, Li R (2016) Mixed alkali neodymium orthoborates: $K_9Li_3Nd_3(BO_3)_7$ and $A_2LiNd(BO_3)_2$ (A = Rb, Cs). Z Anorg Allg Chem 642:424–430

25. Zeng Q, Li R (2010) A new potassium rare earth oxyborate $K_2La_2(BO_3)_2O$. Solid State Sci 12:2144–2147

26. Sheldrick GM (2015) SHELXT–Integrated space-group and crystal-structure determination. Acta Cryst A 71:3–8

27. Hübschle CB, Sheldrick GM, Dittrich B (2011) ShelXle: a Qt graphical user interface for SHELXL. J Appl Crystallogr 44:1281–1284

28. Zhang GC, Li YG, Fu PZ, Pan SL, Chang F, Wu YC (2004) Crystal structure of sodium lanthanum borate Na_3La_2 $(BO_3)_3$. J Synt Cryst 33:490–495

29. Shannon RD (1976) Revised effective ionic radii and systematic studies of interatomic distances in halides and chalcogenides. Acta Crystallogr A 32:751–767

30. Gao J, Li R (2008) Potassium rich rare earth (RE) borates $K_3RE(BO_3)_2$. Solid State Sci 10:26–30

31. Bräuchle S, Huppertz H (2017) Synthesis and structural characterization of $Li_3K_3Y_7(BO_3)_9$. J Solid State Chem 253:242–248

32. Roisnel T, Rodríguez-Carvajal J (1999) WinPLOTR: a windows tool for powder diffraction pattern analysis. In: Materials science forum, 2001. Transtec Publications, pp 118–123

33. Dieke GH, Crosswhite H (1963) The spectra of the doubly and triply ionized rare earths. Appl Opt 2:675–686

34. Kubelka P, Munk F (1931) Ein Beitrag zur Optik der Farbanstriche. Z Tech Phys 12:593–601

35. Tauc J, Grigorovici R, Vancu A (1966) Optical properties and electronic structure of amorphous germanium. Phys Status Solidi B 15:627–637

36. Jin T-T, Zhang Z-J, Zhang H, Zhao J-T (2013) Crystal structure, phase transition and optical properties of v-$PrBO_3$. J Inorg Mater 28:1153–1157

37. Xu D, Zhang F, Sun Y, Yang Z, Lei B, Liu L, Pan S (2017) $LiRb_2LaB_2O_6$: a new rare-earth borate with a MOF-5-like topological structure and a short UV cut-off edge. Dalton Trans 46:193–199

38. Souri D, Tahan ZE (2015) A new method for the determination of optical band gap and the nature of optical transitions in semiconductors. Appl Phys B 119:273–279

39. Kirsch A, Murshed MM, Schowalter M, Rosenauer A, Gesing TM (2016) Nanoparticle precursor into polycrystalline $Bi_2Fe_4O_9$: an evolutionary investigation of structural, morphological, optical, and vibrational properties. J Phys Chem C 120:18831–18840

40. Kirsch A, Murshed MM, Litterst FJ, Gesing TM (2019) Structural, spectroscopic, and thermoanalytic studies on $Bi_2Fe_4O_9$: tunable properties driven by nano-and poly-crystalline states. J Phys Chem C 123:3161–3171

41. Mo Z, Sun Y, Chen H, Zhang P, Zuo D, Liu Y, Li H (2005) Preparation and characterization of a PMMA/Ce(OH)$_3$, Pr$_2$O$_3$/graphite nanosheet composite. Polymer 46:12670–12676

42. Zinatloo-Ajabshir S, Salavati-Niasari M (2015) Nanocrystalline Pr$_6$O$_{11}$: synthesis, characterization, optical and photocatalytic properties. New J Chem 39:3948–3955

43. Steele W, Decius J (1956) Infrared absorption of lanthanum, scandium, and indium borate and the force constants of borate ion. J Chem Phys 25:1184–1188

44. Haberer A, Kaindl R, Huppertz H (2010) Synthesis and crystal structure of the praseodymium orthoborate λ-PrBO$_3$. Z Naturforsch B 65:1206–1212

45. Kuznetsov A, Kokh K, Kononova N, Shevchenko V, Kaneva E, Uralbekov B, Svetlichnyi V, Kokh AE (2020) Synthesis and growth of new rare earth borates KCaR(BO$_3$)$_2$ (R= La, Pr and Nd). J Solid State Chem 282:121091

46. Noirault S, Celerier S, Joubert O, Caldes MT, Piffard Y (2007) Effects of water uptake on the inherently oxygen-deficient compounds Ln$_{26}$O$_{27}$□(BO$_3$)$_8$ (Ln = La, Nd). Inorg Chem 46:9961–9967

Publisher's Note Springer Nature remains neutral with regard to jurisdictional claims in published maps and institutional affiliations.